Halloysite based geopolymers filled with wax microparticles as sustainable building materials with enhanced thermo-mechanical performances

Martina Maria Calvino,[a] Lorenzo Lisuzzo,[a] Giuseppe Cavallaro,[a,b,*] Giuseppe Lazzara,[a,b] Stefana Milioto[a.b]

[a]*Dipartimento di Fisica e Chimica, Università degli Studi di Palermo, Viale delle Scienze, pad. 17, 90128 Palermo, Italy.* giuseppe.cavallaro@unipa.it

[b]*Consorzio Interuniversitario Nazionale per la Scienza e Tecnologia dei Materiali, INSTM, Via G. Giusti, 9, I-50121 Firenze, Italy.*

Abstract

This work proposes a novel protocol for the fabrication of halloysite based geopolymers filled with beeswax microparticles obtained from Pickering emulsions. The actual filling of the microwax into the geopolymers has been demonstrated by using several techniques, including thermal analyses, spectroscopies, microscopies and contact angle experiments. According to the morphological and structural investigations, microwax spherical particles (diameter ranging between ca. 3 and 5 μm) have been homogeneously dispersed within the geopolymeric network conferring excellent properties to the hybrid geopolymers in terms of mechanical performances and heat storage capacity although their low content in the hybrid material. For comparison, we have prepared and characterized hybrid geopolymers obtained by the loading of variable amounts of beeswax within the geopolymeric matrix. Reliable enhancements of the flexural characteristics and heat absorption capacity have been achieved only with a large content of beeswax. Moreover, the removal of microvax and wax from the hybrid geopolymers has been obtained by rinsing with ethanol. The washed geopolymers have been characterized by wettability and water vapour permeability experiments, which have been proved that the beeswax has been removed and the porosity of the materials can be controlled by the initial composition of the hybrid geopolymers.

In conclusion, this paper puts forward an easy strategy to fabricate composite geopolymers with heat storage capacity due to presence of phase change materials (microwax particles) confined in the geopolymeric network. Their enhanced flexural performances make the hybrid geoppolymers suitable as building materials.

Keywords: Geopolymers, Halloysite nanotubes, Pickering emulsion, Beeswax.

1. Introduction

The interest in producing eco-friendly materials from natural resources or industrial by-products has increased in recent years [1,2]. In the construction field, the growing demand for cement production at a large scale further attracted researchers towards its effect on global warming by the emissions of carbon dioxide [3]. In this regard, research is currently focused on geopolymeric materials that offer new perspectives in environmental remediation technologies and can be synthesized from various industrial by-products such as fly rice husk ashes [4], furnace slag [5] and natural clays [6].

Geopolymers are inorganic polymeric materials that possess an amorphous network of aluminosilicates. They are obtained from a geopolymerization process with an alkaline activating solution leading to the formation of three-dimensional structures with Si–O–Al bonds. Poli-silicon-oxo-aluminate network is composed by SiO_4 and AlO_4 groups with a bridging oxygen between silicon and aluminum atoms and negative charges of AlO_4 groups that are typically balanced by sodium (Na^+) or potassium (K^+) cations. Geopolymers have the empirical formula $M_n[-(SiO_2)_z-AlO_2]\cdot wH_2O$ where M is a cation (Na^+, K^+ or Ca^{2+}), n is the degree of polycondensation, z is 1, 2, or 3 and w is the number of water molecules. There are three classes of geopolymers on dependence of of the Si/Al ratio: polysialate (–Si–O–Al–O), polysialate-siloxo (–Si–O–Al–O–Si–O–) and polysialate-disiloxo (–Si–O–Al–O–Si–O– Si–O) for Si/Al ratio equals to 1, 2 and 3, respectively [7]. Once the precursors have been completely reacted, the geopolymeric bulk structure is intrinsically micro and mesoporous. The amount of these porosities (ranging from 30 to 60 vol%) is related to the system's composition and to the specific Si/Al ratio. Furthermore, also highly porous geopolymers and geopolymer foams (porosity > 70vol%) are getting attention due to their physical properties in terms of high thermal and chemical stability and other applications that cannot be pursued using the traditional geopolymer matrix. As examples, these materials can be employed as adsorbents [8,9], acoustic and thermal insulators [10] and adsorbents for heavy metals [11]. Porosity can be introduced

on purpose into the micro- and meso-porous geopolymer matrix by removing a “sacrificial” material from its network [12].

The microstructure of geopolymer mortar can be improved by nanoparticles [13] due to their ability to be uniformly dispersed in the binder paste. Nowadays, nanoparticles are widely employed in combination with several traditional materials in order to modify and improve specific properties, developing modern multifunctional products. For instance, nanoclays are suitable as additives of cement concretes to enhance their mechanical performances because of their peculiar physical chemistry, morphology, and charge characteristics. Among clay nanoparticles, halloysite nanotubes (HNTs) are emerging natural aluminosilicates belonging to the category of phyllosilicates with the chemical formula of $Al_2Si_2O_5(OH)_4 \cdot 2H_2O$. These nanomaterials are widely used in for industrial and biotechnological applications because of their low cost, ecocompatibility and low toxicity [14–17]. Halloysite nanotubes have a hollow tubular structure and an inner surface consisting of octahedral gibbsite (Al–OH), while the outer surface is formed by siloxanes (Si–O–Si). The sizes of the nanotubes depend on their natural source of extraction [18]. The tube length is 1-2 μm, external diameter is between 50 and 200 nm, while the internal diameter ranges between 15 and 50 nm. The halloysite surfaces charges are influenced by pH due to the ionization equilibria of the Si–O groups (external surface) and Al-OH groups (internal surface). Consequently, the inner and the outer surfaces are positively and negatively charged, respectively, for pH ranging between 2 and 10. On this basis, ionic molecules can be used for the specific surface functionalization to improve the HNTs reactivity and selectivity and/or to drive the encapsulation of functional species within the halloysite lumen [19,20]. On this basis, halloysite can be exploited in several fields, such as adsorbent for wastewater remediation [21–26], catalytic support [21,22,27–31], drug delivery [32–37], biomedicine [38–40], cosmetics [41,42] and pharmaceutics [43,44]. Chemically, halloysite is very similar to kaolinite, which does not possess the two water molecules located between the tetrahedral layer and the octahedral one. These clays also have different morphology being that kaolinite is a platy nanoparticle with a basic unit of a two-dimensional layer of silicate groups bonded to a layer of aluminate groups.

Both halloysite and kaolinite can be used as aluminosilicate precursors in geopolymer synthesis as reported in literature [45–47]. Notably, metakaolin obtained from kaolinite containing traces of halloysite was investigated [48]. It was observed that the presence of HNTs leads to a higher silicon and aluminum dissolution and, consequently, to an increase of the geopolymerization rate with respect to the pure kaolinite improving the reactivity [49]. Halloysite can also act as an interfacial active particle to stabilize the resulting Pickering emulsions [50–53].

The development of new hybrid materials drives to realize products that can have different properties by tuning the chemical composition of the two phases [54]. As reported in literature, the presence of additives in geopolymers can lead to an enhancement of their physico-chemical properties. In the last decade, both organic and inorganic additives, such as micro silica, micro fibrils and carbon fibers, were successfully employed to improve the mechanical performances and the thermal resistance of geopolymers as well to enhance the geopolymerization reaction for concrete application [55–57]. For instance, nano-SiO_2 can improve the microstructure, hardening properties and compressive strength of fly ash-based geopolymers [58]. It was demonstrated that their durability properties can be extended compared to ordinary geopolymeric concrete also by employing bio-additives [59,60]. The effect of silica fume, alumina, quartz powder, fibres and nanomaterials as additives was explored mostly on slag or fly ash based geopolymers [61] but a deeper investigation on clay based geopolymers is needed. Here, we propose new hybrid halloysite-based geopolymers with microwax particles obtained from dried Pickering emulsion. For comparison, we prepared hybrid geopolymers filled with beeswax at variable composition. Within this, it should be noted that the nanoencapsulation of phase change materials was recently explored to fabricate advanced thermal storage systems [62–64]. The final products represent the starting point for the design of hybrid and green geopolymers including confined microwax (phase change material) with a high thermal capacity that can be strategic for energy storage applications. The filled geopolymers could be employed for construction industry as a green concrete alternative to the traditional cements reducing the greenhouse gas emissions.

2. Materials and Methods

2.1 Materials

Halloysite nanotubes (HNTs), beeswax, sodium hydroxide and Nile Red are Sigma Aldrich products. Ethanol (96%) is from Honeywell.

2.2 Preparation of Pickering emulsions

The Pickering emulsion was prepared using a similar protocol reported elsewhere for halloysite/paraffin.[65] Firstly, 0.3 grams of solid beeswax were added to 100 ml of water under magnetic stirring at 80 °C. After wax was completely dispersed, 1.2 grams of halloysite nanotubes were added to the emulsion that was subjected to ultrasounds for 10 minutes. The obtained dispersion was magnetically stirred for 30 minutes at 80 °C. Then, the heating system was turned off and the emulsion was kept under stirring until the temperature of 25 °C was achieved. This strategy allowed us to obtain solid stable wax microparticles surrounded by halloysite nanotubes. According to literature [65], particles of well-defined spherical shape of about ten micrometers can be obtained using the mentioned protocol. After 24 hours, the resulting Pickering emulsion was stable at room temperature, and it was dried under vacuum to obtain the powder.

2.3 Preparation of Geopolymers filled with wax and microwax particles

Firstly, we dried the Pickering emulsion under vacuum at room temperature allowing us to obtain microwax spheres. Then, the microparticles were mixed with the same amount of pure halloysite nanotubes and, subsequently, with the alkaline activating solution (NaOH 12 M). Sodium cations (Na^+) balance the equal negative charges of four-coordinated Al ($[AlO_4]^-$) in the geopolymeric network. Accordingly, the NaOH/HNTs ratio was set to 1. After mixing at 25 °C, a homogeneous slurry was obtained, and it was placed into a plastic mold and cured at 50 °C for 48 hours.

For comparison, a very similar procedure was carried out to prepare geopolymers filled with beeswax at different wax/halloysite ratios, $R_{wax/HNT}$ (Table 1) and an unfilled conventional geopolymer. Once

added the alkaline activator solution to halloysite nanotubes, solid beeswax was incorporated under heating at 70°C until we obtained a homogeneous geopolymer slurry (Figure 1). The last step for all samples was curing at 50 °C for 48 hours in a rectangular plastic mold.

A schematic illustration of the preparation protocol developed for the filled geopolymers is displayed in Figure 1.

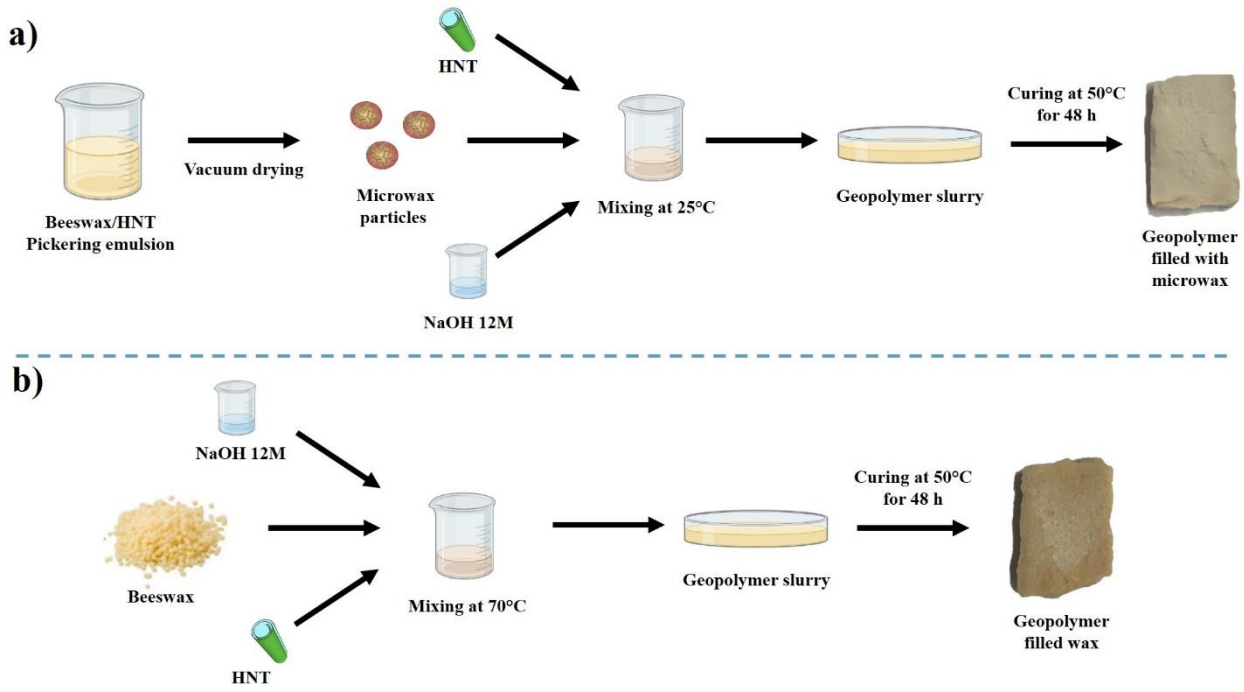

Figure 1. Schematic representation of the preparation protocol for geopolymer filled with microwax particles (a) and wax (b).

Table 1. List of the geopolymer samples with the percentages of each components.

Sample	$R_{wax/HNT}$	HNT / wt %	Beeswax / wt %	NaOH / wt %
GP	0	50	0	50
GP_wax	0.25	44.4	11.2	44.4
GP_wax	0.5	40	20	40
GP_wax	0.75	36.4	27.2	36.4
GP_wax	1	33.3	33.4	33.3
GP_microwax	0.07*	48.3	3.4	48.3

*calculated from TGA

2.4 Methods

2.4.1 Thermogravimetric Analysis (TGA)

Thermogravimetric experiments were performed by means of a Q5000 IR apparatus (TA Instruments) under inert atmosphere using nitrogen flows of 25 and 10 cm^3 min^{-1} for the sample and the balance, respectively. Each sample (ca. 10 mg) was heated in a platinum pan from room temperature to 700 °C with a scanning rate of 20 °C min^{-1}.

2.4.2 Differential scanning calorimetry (DSC)

Differential scanning calorimetry (DSC) measurements were carried out with the TA Instruments DSC (2920 CE) under nitrogen flow atmosphere (flow rate of 60 cm^3 min^{-1}) from − 20 to 110 °C with a heating rate of 10 °C min^{-1}. We used aluminum pans, while the mass sample was ca. 2 mg. The melting temperature (T_m) of beeswax in the geopolymer materials was calculated and defined as the maximum of the endothermic peak occurring in the range between 30 and 70 °C. The enthalpy of the melting process was estimated by the integration of the peaks and expressed as Joule per gram of beeswax. The calibration was performed by using the indium as standard.

2.4.3 FT-IR spectroscopy

FT-IR spectra in KBr pellets were measured using a Perkin-Elmer FT-IR Spectrum One instrument in the spectral region between 4000 and 400 cm^{-1}. An average of 30 scans per sample using a nominal resolution of 4 cm^{-1} was registered.

2.4.4 X-ray Diffraction (XRD)

The patterns were obtained from an X-ray diffractometer (Rigaku, MiniFlex) with a CuKa radiation source including a nickel filter and working at 40 kV and 15 mA. The wavelength of the X-ray beam was 1.5406 Å, and the layer spacing of the samples was calculated by the and Bragg's equation, which can be expressed as

$$n\lambda = 2d\sin\theta \quad (1)$$

where θ is the angle that the outgoing beam forms with the crystalline layer, λ is the wavelength of the radiation, d is the distance between two adjacent layers and n can be 1,2 or 3.

The angle for scanning was ranged from 2 ° to 70 ° with a rate of 20 ° min^{-1} and a step of 0.02°.

2.4.5 Nile Red essay

1 mg of Nile red was dissolved in 10 mL of ethanol and stirred until the compound was completely solubilized. One drop of this solution was used to cover all the samples that, after drying in the oven for 10 minutes, were observed under UV-lamp irradiation in a dark room.

2.4.6 Water contact angle measurements

Water contact angle measurements were carried out by using an optical contact angle apparatus (OCA 20, Data Physics Instruments, Filderstadt, Germany) implemented with a video measuring system with a high-resolution CCD camera and a high-performance digitizing adapter. Data acquisition was conducted by SCA 20 software (Data Physics Instruments, Filderstadt, Germany). The water contact angle in air was measured through the sessile drop method by gently placing a water droplet of 10 ± 0.5 μL onto the surface of the geopolymer block by a syringe pointed vertically down onto the sample. The tests were conducted at a temperature of 25.0 ± 0.1 °C. Images were collected at a rate of 25 frames per second starting from the deposition of the drop to 60 s.

2.4.7 Scanning Electron Microscopy (SEM)

morphological investigations were conducted by a SEM microscope (Desktop SEM Phenom PRO X PHENOM) with magnification field 160-350.000x and voltage in the range between 4.8 and 20.5 kV. As concerns SEM analyses, each sample was preliminarily coated with gold to avoid charging effects under an electron beam.

2.4.8 Water vapour permeability analysis

Water vapor permeability tests were performed, at a temperature of 28 ± 1 °C and relative humidity of 30 ± 2 % in a desiccator, which contained a saturated solution of calcium chloride dehydrate and twelve bottles (50 mL, 2 cm inner diameter) full of water. A thermohygrometer was placed inside the equipment to check the environmental parameters. Geopolymers were fixed on the top of each bottle and the water transferred through the materials, and absorbed by the desiccant, was determined from the weight loss of the bottle every 24 hours for 10 days. Water vapor transmission rate (WVTR) and water vapor permeability were calculated by applying the following equations.

$$WVTR = (\Delta m/\Delta t A) \quad (2)$$

$$WVP = WVTR\ (L/\Delta p) \quad (3)$$

where $\Delta m/\Delta t$ is the slope of each line obtained from the weight loss of samples over time (g/h), A is the exposed surface area of the sample (m^2), L is the thickness of the sample (m) and Δp is the difference of partial pressure (Pa) between saturation solution at 30% of relative humidity and saturation water vapor pressure at a temperature of 28 °C.

2.4.9 Thermal Imaging

A FLIR E6-XT infrared camera (FLIR Commercial Systems Inc.) with 240 x 180 pixels and a temperature range from -20 to 550 °C was employed for thermal imaging analysis. Samples were placed vertically on an electric hot plate and heated to 60°C. Thermal images were analyzed through FLIR Tools software.

2.4.10 Dynamic Mechanical Analysis

Dynamic mechanical analysis was conducted with a DMA Q800 (TA Instruments) and specifically by using a three-point bending clamp at 25 °C. The ramp force was set at 0.2 N min^{-1} from 0.01 to 10 N.

2.4.11 Helium Pycnometer

The Accupyc 1330 Micromeritics gas pycnometer was employed to determine the skeletal density and the porosity of the geopolymeric samples (before and after the washing by ethanol) by measuring the pressure change of helium (purity of 99.995 %) in a calibrated volume. The apparatus has a 10 cm^3 cell suitable for the analysis of small specimens of the geopolymers. Standards for the volume calibration (balls purchased from Micromeritics, V_{cal} = 6.371684 cm^3) were used. The measurements were carried out at 25°C.

3. Results and Discussion

Preliminarily investigations of geopolymers were carried out by thermal analyses (TGA and DSC) and spectroscopies (XRD and FT-IR) to evaluate the actual formation of the geopolymeric network. The thermal behavior and the structural characteristics of geopolymers and their corresponding precursor (Halloysite) will be presented and discussed in the following paragraph.

3.1 Characterization of geopolymers: thermal analyses and spectroscopies

Figure 2 compares the thermogravimetric (TG) curves of geopolymers with pristine halloysite.

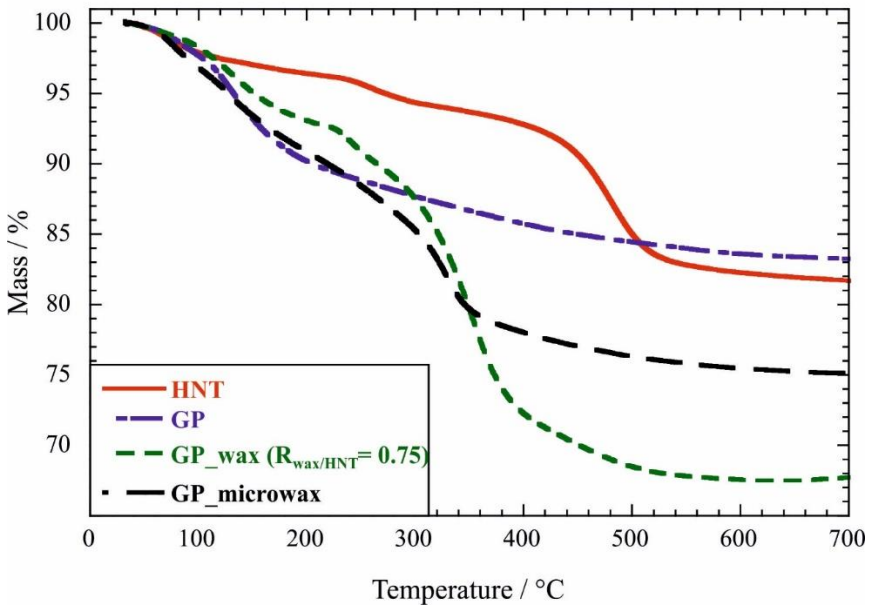

Figure 2. Thermogravimetric curves of HNT, GP, GP_wax ($R_{wax/HNT}$ = 0.75) and GP_microwax.

We observed that pristine halloysite presents an evident mass loss in the range between 400 and 500 °C due to the expulsion of the interlayer water molecules from the HNT structure [66]. As expected, this signal was not detected in all geopolymers due to the structural changes of halloysite clay after the geopolymerization reaction. On the other hand, the geopolymer samples showed a significant mass reduction (ca. 10 wt %) from 25 to 200 °C as a consequence of the evaporation process of physically adsorbed water molecules.

The conventional geopolymer (sample GP) did not evidence any further mass losses within the investigated temperature range. On the other hand, GP_wax and GP_microwax evidenced a clear mass change at ca. 350 °C because of thermal decomposition of beeswax filled within the geopolymeric network. Accordingly, their residual masses at 700 °C (ca. 68 and 75 wt% for GP_wax and GP_microwax, respectively) are lower than the conventional geopolymer (ca. 80 wt%).

Moreover, thermogravimetric data provided the weight fraction of wax in GP_microwax calculated as follows

$$\chi(\text{wax}) = (MD_{700P} - MD_{700HNT})/(MD_{700wax} - MD_{700HNT}) \quad (4)$$

where MD_{700P}, MD_{700HNT} and MD_{700wax} refer to degraded matters at 700 °C of wax/halloysite particles, halloysite and beeswax, respectively. From the calculated χ(wax) value, we determined the wax/HNT mass ratio in the GP_microwax sample (Table 1).

The presence of crystalline beeswax within the filled geopolymers was confirmed by DSC curves (see Supplementary Material),which showed endothermic peaks at ca. 65-70 °C due to the melting of the organic macromolecules. According to literature [67], this signal is related to the solid-liquid transition, while the slight shoulder occurring at a lower temperature (ca. 30-40 °C) to a solid-solid transition. We estimated the melting temperature T_m of the filled beeswax by the minimum of the DSC peaks. Interestingly, the T_m of GP_microwax is larger with respect to those of GP_wax samples (Table 2). Furthermore, the integration of the peaks provided the enthalpies (ΔH_m) of the melting process (Table 2).

Table 2. Thermal parameters of beeswax and geopolymer samples

Sample	$R_{wax/HNT}$	ΔH/ J g^{-1}	T_m / °C
Beeswax	/	205	66.2
GP	/	/	/
GP_wax	0.25	193	65.5
GP_wax	0.5	188	65.8
GP_wax	0.75	127	64.5
GP_wax	1	105	64.7
GP_microwax	0.07	191	70.0

The ΔH_m were expressed in J g^{-1} of beeswax, which is the component providing the melting signal. As described by Lvov et al. [68] the wax crystallinity is partially destroyed by halloysite nanotubes. As a matter of fact, the obtained values indicate a reduction of the enthalpy by increasing the wax/HNT ratio (Figure 3) indicating a decrease of the wax crystallinity in the geopolymeric network.

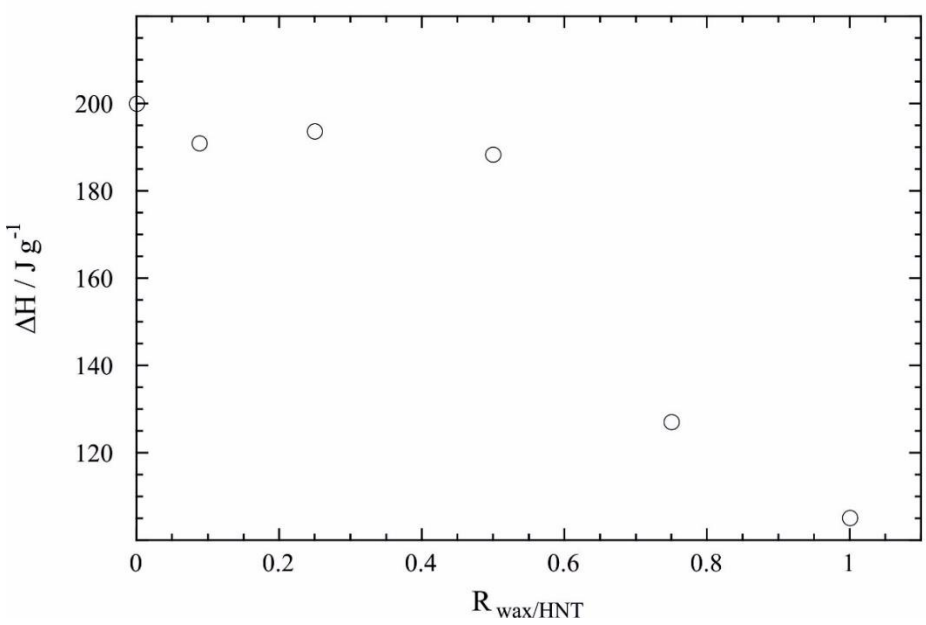

Figure 3. Enthalpy of the wax melting process for filled geopolymers with variable wax/HNT ratio.

FT-IR spectra for HNT, GP and GP_wax are illustrated in Figure 4 and a detailed assignment of all the identified peaks is reported in Supplementary Material (Table 1S). According to literature [67,69], halloysite nanotubes possess two characteristic bands at 3698 and 3608 cm^{-1} representing the stretching of hydroxyl groups in the inner and outer surfaces. The signals at 1093 and 1028 cm^{-1}

are assigned to the stretching vibrations of apical Si–O and Si–O–Si, respectively. The peaks at 796 cm^{-1} can be attributed to the symmetric stretching of Si–O–Si, while the signals at 692 and 753 cm^{-1} are related to the perpendicular stretching of Si–O–Al. Moreover, the band observed at 533 cm^{-1} reflects the deformation vibration of Al–O–Si.

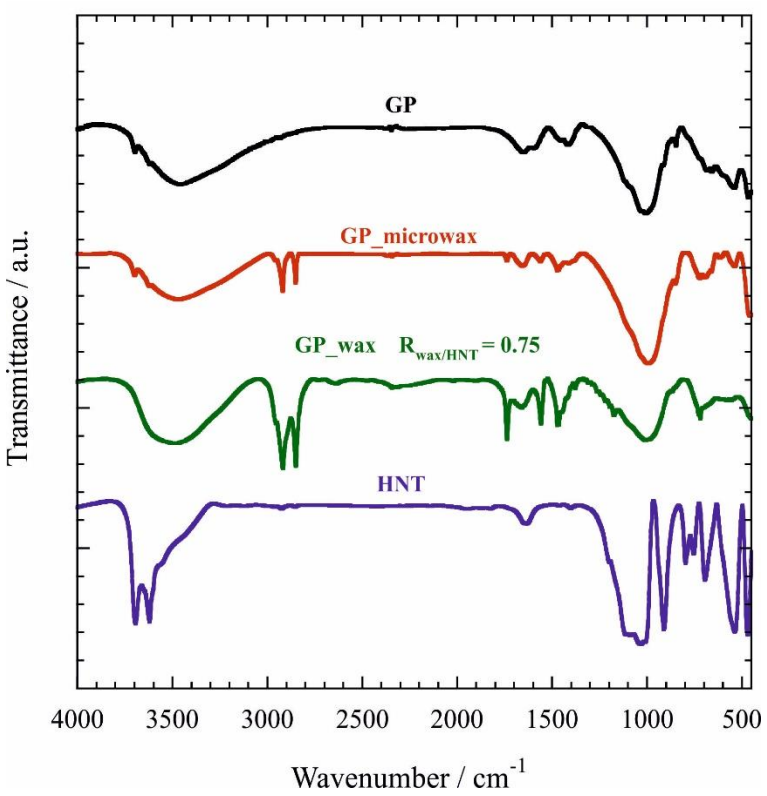

Figure 4. FT-IR spectra of HNT, GP, GP_microwax and GP_wax ($R_{wax/HNT}$ = 0.75).

On the other hand, geopolymerization influences the position of the peaks leading to the disappearance of the aforementioned characteristic signals of halloysite at ca. 3600 cm^{-1}. FTIR spectra of geopolymers (Figure 4) present bands at 3458 and 1658 cm^{-1} related to the –OH stretching and bending vibrations of water's hydration.[70] Figure 4 showed the often called "main band" between 1025 and 1015 cm^{-1} attributed to Si−O−T (T = tetrahedral Si or Al) asymmetric stretching vibration. Hajimohammadi et al.[71] stated that this band depends on connectivity and Si/Al ratio. Moreover, they revealed that it can be attributed to the presence of predominantly Si–O–Al bonds. It can be evidenced that there is a shift of this band from 1044 cm^{-1} in HNT to 1012 cm^{-1}

in geopolymers that is related to the degree of geopolymerization. As reported in literature, this shift is caused by the increased substitution of Al in the tetrahedral silicate network [71–73]. Namely, the higher Si/Al ratios, the higher the silicon content and the band will be moved to higher wavenumbers as a result of reorganization and condensation with higher Si contribution to the gel structure.

The bands at 718 and 450 cm^{-1} can be associated with Si−O−Al bending vibration and in-plane Si−O−Si stretching vibration, respectively [74]. Furthermore, we observed additional FT-IR signals in the filled geopolymers with variable intensities on dependence of the wax/HNT ratio attributed to the presence of beeswax [75]. The presence of beeswax in the geopolymer structure was confirmed by the peaks at 2920 and 2848 cm^{-1} (CH_2 asymmetric and symmetric stretching vibrations, respectively), 1737 cm^{-1} (C=O stretching vibration) as well as 1472 and 720 cm^{-1} (scissor deformation vibration and rocking vibrations of CH_2 groups, respectively).

Structural differences after geopolymerization are evidenced by the diffractometer. XRD patterns of the geopolymers are illustrated in Figure 5. The diffractogram of HNT exhibits the first reflection at $2\theta = 11.8$ ° in agreement with the dehydrated form of halloysite (basal spacing of 7.47 Å). Besides, the reflections at 19.9 and 24.3° can be related to the basal spacing of 4.4 and 3.6 Å, respectively. These signals were not detected in both the unfilled and filled geopolymers, which exhibited a broad reflection band from 20 to 40° (2θ), highlighting the formation of an amorphous geopolymeric network. In addition, all the geopolymers evidenced reflections attributed to quartz [76,77] and traces of hydrosodalite phase that could appear after alkali activation [78]. As shown in Figure 5, both GP_wax and GP_microwax samples evidenced the reflection signals (19.1, 21.2, 23.6, 29.7 and 39.9°) attributed to the orthorhombic structure of beeswax corresponding to d equals to 4.6, 4.2, 3.8, 3.1 and 2.3 Å respectively.[79–81] It should be noted that the intensities of these peaks are reduced in the filled geopolymers compared to those of pure beeswax. These results are consistent with the reduction of the crystallinity of beeswax, as evidenced in DSC data (Table 2).

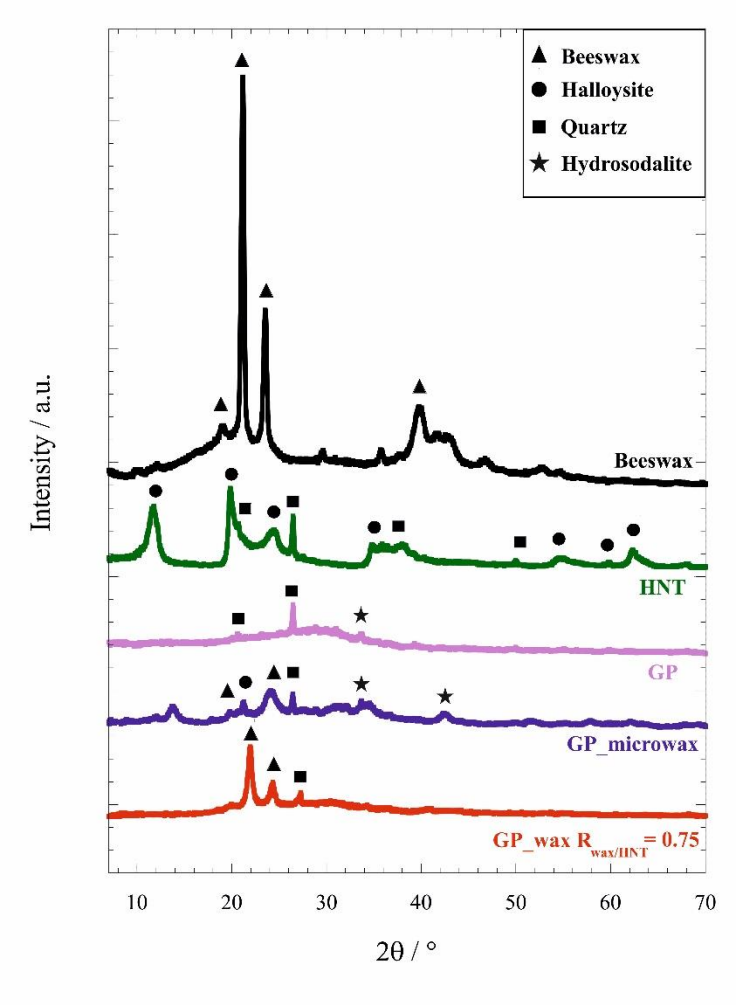

Figure 5. Diffractograms of Beeswax, HNT, GP, GP_microwax and GP_wax $R_{wax/HNT}$ = 0.75.

3.2 Morphology and surface properties of filled geopolymers

3.2.1 Nile Red essay

The filling of geopolymers with wax and wax microparticles was demonstrated using the qualitative essay of hydrophobicity by Nile Red. It was used as a fluorescent probe because this molecule is highly emissive in hydrophobic environments and it shows a red luminescence under UV light irradiation. As shown in Figure 6, the pristine geopolymer did not evidence any luminescence in agreement with its hydrophilic character. In contrast, the filled geopolymers are luminescent because of the presence of the hydrophobic beeswax. Interestingly, GP_microwax exhibited a high luminescence although the small amount of wax entrapped within the geopolymeric network. The

latter could be an indication of the high dispersibility of the wax microparticles within the geopolymeric matrix.

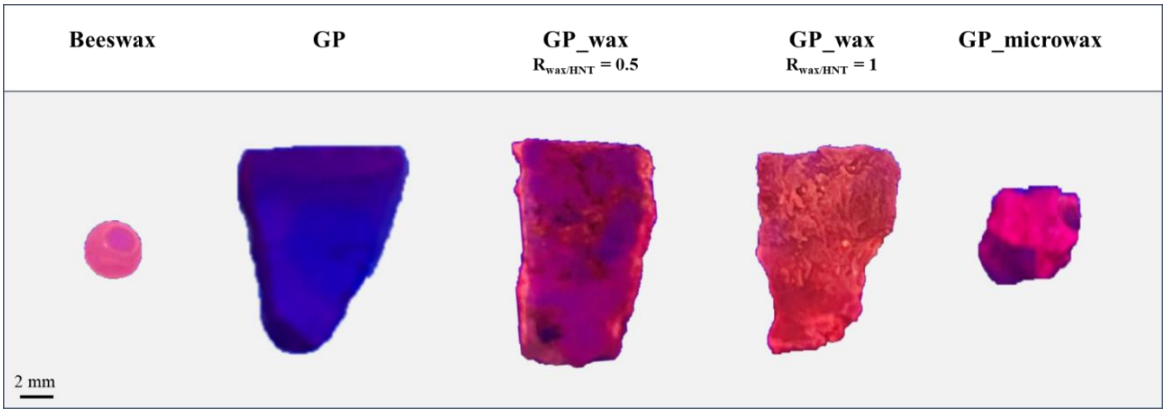

Figure 6. Nile Red essay for Beeswax, GP, GP_wax ($R_{wax/HNT}$ = 0.5 and 1) and GP_microwax.

3.2.2 SEM analyses

SEM images of GP, GP_wax ($R_{wax/HNT}$= 1) and GP_microwax are displayed in Figure 7. We observed that the filling with both wax and microwax particles induces significant changes in the morphology of the geopolymer. Specifically, GP showed a denser and more homogeneous matrix with respect to those of filled geopolymers (Figure 7a). GP evidenced the presence of few halloysite nanotubes embedded within the geopolymeric matrix that can be considered as residual precursors of the geopolymerization. GP_wax exhibited an irregular morphology with the wax randomly distributed within the geopolymer network (Figure 7b). In contrast, GP_microwax showed a uniform distribution of the wax microparticles that reduced the compactness of the geopolymer (Figure 7c). It should be evidenced that the wax microparticles present a spherical shape with a diameter ranging between 3 and 5 μm. As shown in Figure 7d, the surface of the wax microparticles is covered by spherical nanoparticles (diameter of ca. 400 nm) of halloysite, which lost its tubular morphology as a consequence of the alkaline activation.

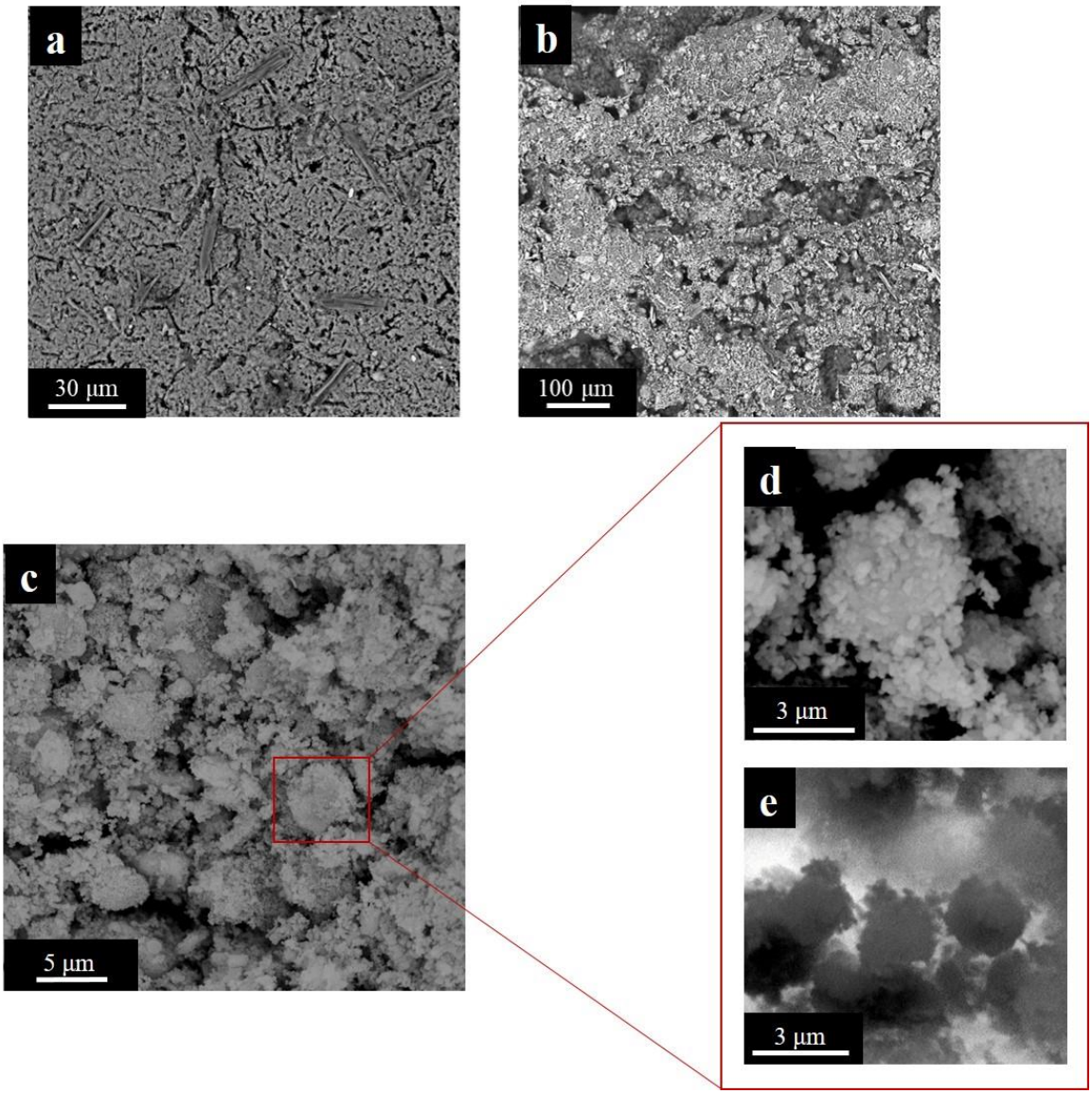

Figure 7. SEM images of GP (a), GP_wax ($R_{wax/HNT}$ = 1) (b) and GP_microwax (c-e).

3.2.3 Wettability

The filling of geopolymers with both wax and microwax induced significant changes in the wettability properties (Figure 8). Due to its very hydrophilic character, the initial water contact angle of HNTs based geopolymer was not measureable. On the other hand, we determined the water contact angle values just after their deposition on both GP_wax and GP_microwax materials (Table 3). Accordingly, we can state that the filling of the geopolymeric network generated the hydrophobization of the surface, which can be related to the variation of its chemical composition (being wax hydrophobic) as well as to the enhancement of its roughness. The latter is consistent with

SEM images (Figure 7). Similar observations were done for hydrophilic films loaded with hydrophobic coffee particles [82].

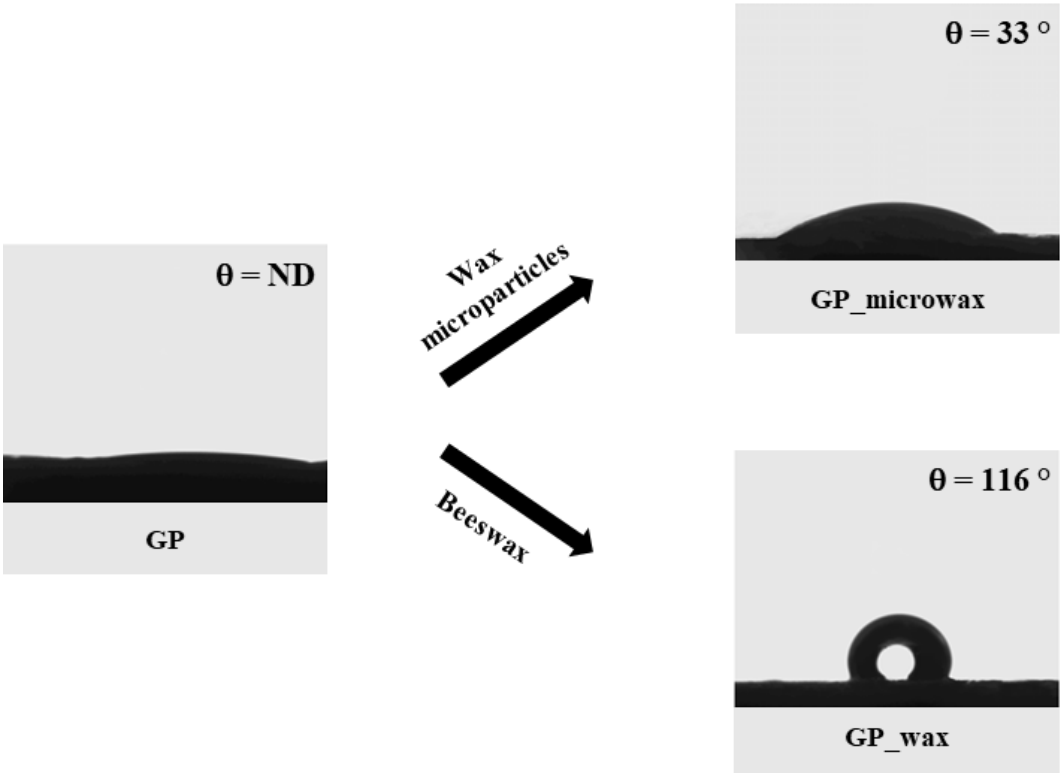

Figure 8. Images of the water droplets contact just after their deposition on GP, GP_microwax and GP_wax ($R_{wax/HNT}$ = 1).

It should be noted that the surface hydrophobization generated by wax microparticles is lower compared to that observed in GP_wax materials, which exhibited larger contact angle values by increasing the wax content (Table 3). Namely, increasing the percentage of wax causes a relevant change of θ_i values (initial contact angle) up to 116°, due to the more hydrophobic character (Table 3). These observations could indicate that the hydrophobization of the geopolymer is predominantly caused by variations of the surface chemistry.

Additionally, we investigated the kinetic evolution of the water contact angle using the following equation

$$\theta = \theta_i \exp(-k_\theta t^n) \quad (5)$$

where θ_i is the initial contact angle extrapolated at zero time, k_θ estimates the process rate, and n has fractional values according to the occurrence of absorption and spreading i.e. n = 0 for pure absorption and n = 1 for pure spreading. As example, the comparison between the experimental and calculated data for GP_wax ($R_{wax/HNT}$ = 1) is presented in Figure 9, while the obtained fitting parameters for all the filled geopolymers are listed in Table 3.

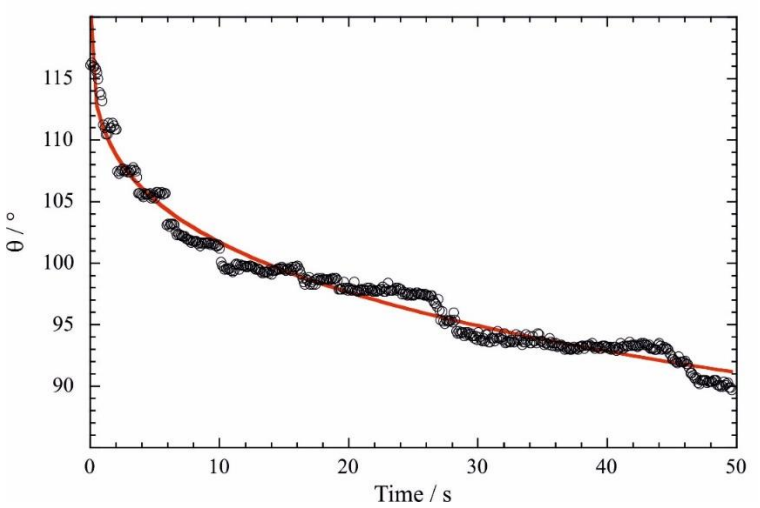

Figure 9. Water contact angle as a function of time for GP_wax ($R_{wax/HNT}$ = 1). The red line represents the fitting according to the equation 5.

Table 3. Fitting parameters obtained from the kinetic analysis of water contact angle data.

Sample	$R_{wax/HNT}$	θ_i / °	k_θ / s^{-1}	n
GP	0	ND	ND	ND
GP_microwax	0.07	33.4	0.018 ± 0.002	0.63 ± 0.03
GP_wax	0.25	61.8	0.17 ± 0.01	0.22 ± 0.01
GP_wax	0.5	77.6	0.020 ± 0.003	0.67 ± 0.03
GP_wax	0.75	82.3	0.058 ± 0.003	0.34 ± 0.09
GP_wax	1	116.0	0.086 ± 0.004	0.303 ± 0.009

3.3 Heat storage capacity of filled geopolymers

The heat storage capacity of GP, GP_wax and GP_microwax was studied by using thermal images of geopolymeric materials placed on a support kept at 60 °C, which guarantees that the wax melting was reached. Therefore, microwax particles and wax can act as phase change fillers absorbing

thermal energy. As example, Figure 10a shows the thermal images of GP_microwax compared to GP_wax ($R_{wax/HNT}$ = 0.25). Based on the analysis of the thermal images, we determined the temperature gradient on dependence of the distance from the support. The obtained trends are presented in Figure 10b. As expected, the gradient temperature shows negative values because of the heat dissipation along the geopolymer material for all the investigated samples. As a general result, exponential decreasing trends were detected. It should be noted that GP and GP_wax ($R_{wax/HNT}$ = 0.25) exhibit similar trends indicating that the wax addition did not alter the heat absorption capacity of the geopolymer. Accordingly, the gradient temperature values at the top of the sample (5 mm of distance from the support) were -10.99 and -11.06 °C for GP and GP_wax ($R_{wax/HNT}$ = 0.25), respectively. On the other hand, larger amount of wax loaded in the geopolymeric network (GP_wax at $R_{wax/HNT}$ = 0.75) affected the heat absorption behaviour of the geopolymer being that the gradient temperature at 5 mm was - 4.07 °C. Interestingly, filling with wax microparticles significantly reduced the gradient temperature (- 7.42 °C at the top of the GP_microwax sample) despite the very low amount of wax entrapped within the geopolymeric network. In this regard, we should remind that GP_microwax presents $R_{wax/HNT}$ equals to 0.07 (Table 1). This effect could be due to the uniform distribution of wax microparticles within the geopolymeric matrix.

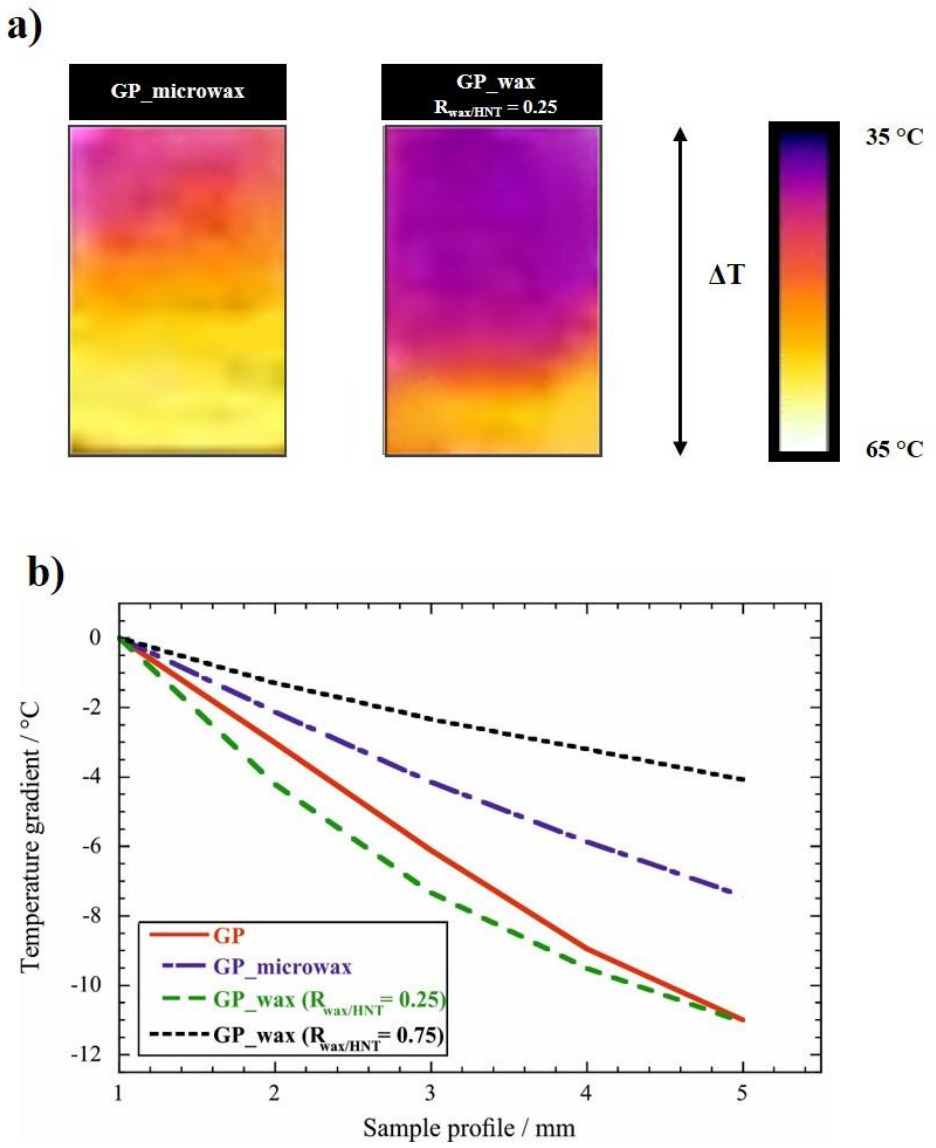

Figure 10. Thermal images of GP_microwax and GP_wax ($R_{wax/HNT}$ = 0.25) (a). Temperature gradient as a function of the sample profile for GP, GP_microwax and GP_wax ($R_{wax/HNT}$ = 0.25 and 0.75) (b).

3.4 Mechanical performances of filled geopolymers

We investigated the effects of wax and microwax particles loadings on the flexural properties of geopolymers. Figure 11a compares the stress vs strain curves of GP, GP_microwax and GP_wax at variable compositions ($R_{wax/HNT}$ = 0.25 and 0.75). Compared to the unfilled geopolymer, GP_microwax and GP_wax materials showed lower elastic modulus and stress at breaking point values, while the ultimate elongation was enhanced (Table 4). On this basis, we can state that the loading with both wax and microwax enhanced the flexibility of the geopolymers. It should be noted

that GP_microwax presents higher stiffness with low deformation due to the homogeneous distribution of microwax particles into the geopolymeric matrix. Compared to the GP material, the elastic modulus of GP filled with wax microparticles is ca. 6 times lower, while the ultimate elongation was enhanced by a factor of 6. Furthermore, the integration of stress vs strain curves allowed us to estimate the stored energy at the breaking point. As shown in Figure 11b, GP_wax ($R_{wax/HNT}$ = 0.75) possesses the strongest capacity to store energy during the flexural tests. Interestingly, the energy requested for the breaking of GP_microwax is higher with respect to that of GP_wax ($R_{wax/HNT}$ = 0.25) despite its lower amount of wax due to the homogeneous filling of the microparticles within the geopolymeric network. Compared to the unfilled geopolymer, the stored energy up to breaking was enhanced by factors of ca. 2.5 and 5 for GP_wax ($R_{wax/HNT}$ = 0.25) and GP_microwax, respectively. It should be noted that GP_microwax presents a wax loading lower of ca. 3 times with respect to that of GP_wax ($R_{wax/HNT}$ = 0.25).

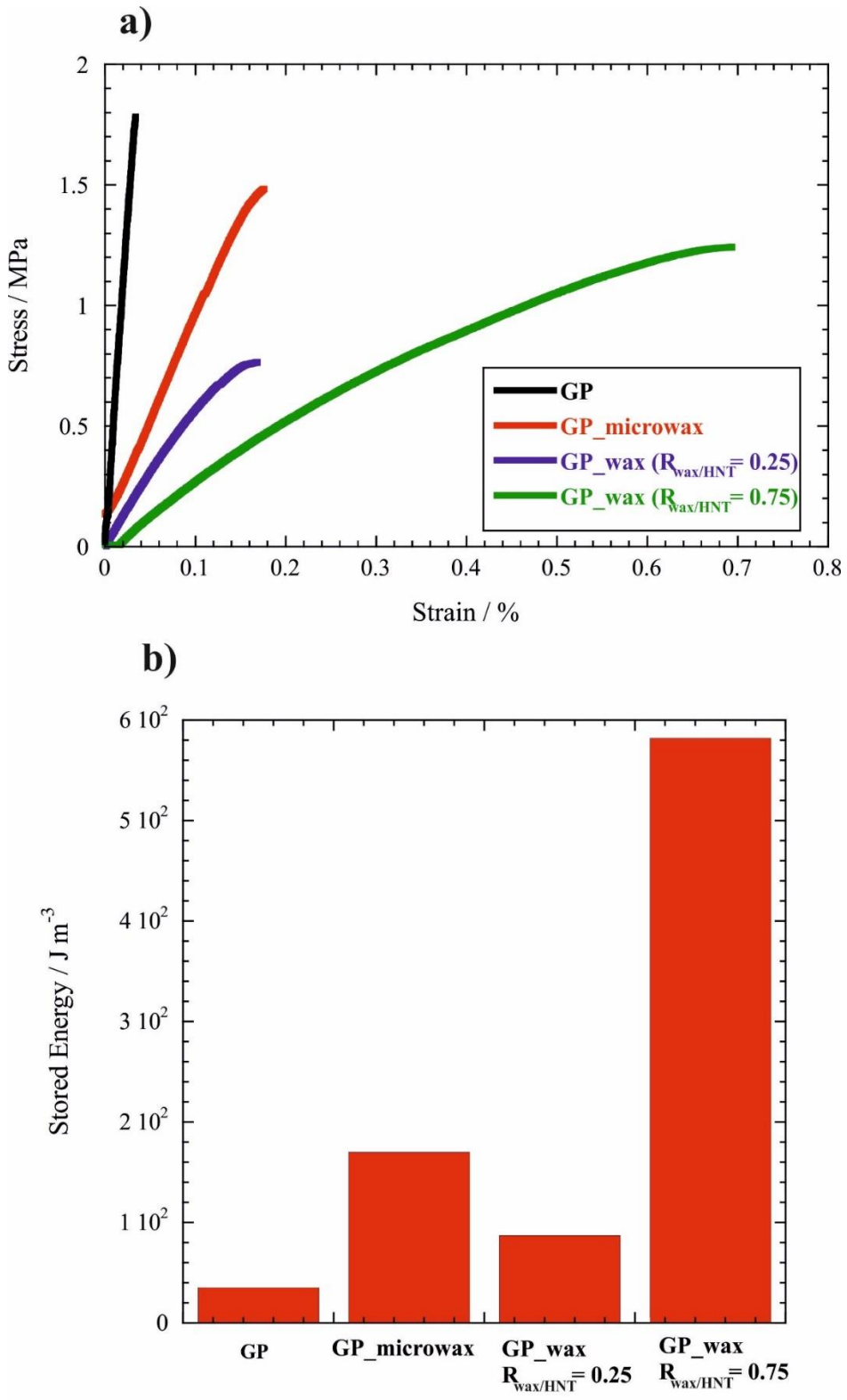

Figure 11. Stress vs strain curves (a) and stored energies up to breaking (b) for GP, GP_microwax, GP_wax ($R_{wax/HNT}$ = 0.25 and 0.75). The relative error for stored energies up to breaking is 2%.

Table 4. Elastic modulus, stress and elongation at breaking point.[a]

Sample	Elastic Modulus / MPa	Stress at Breaking point / MPa	Elongation at Breaking point / %
GP	5425	1.8	0.03
GP_microwax	863	1.5	0.18
GP_wax ($R_{wax/HNT}$ = 0.25)	603	0.8	0.17
GP_wax ($R_{wax/HNT}$ = 0.75)	261	1.2	0.69

[a]The relative error is 2%.

3.5 Wax removal from filled geopolymers by rinsing with ethanol

Filled geopolymers were rinsed with ethanol to remove wax from the geopolymeric network and consequently, to obtain materials with controlled porosity. The actual removal of wax was highlighted by Nile Red essay and TG curves, which showed that washed geopolymers did not present any mass loss in the temperature range between 300 and 400 °C (see Supplementary Material). Accordingly, Nile Red essay evidenced that GP_wax materials are not luminescent after their washing by ethanol (Figure 12a).

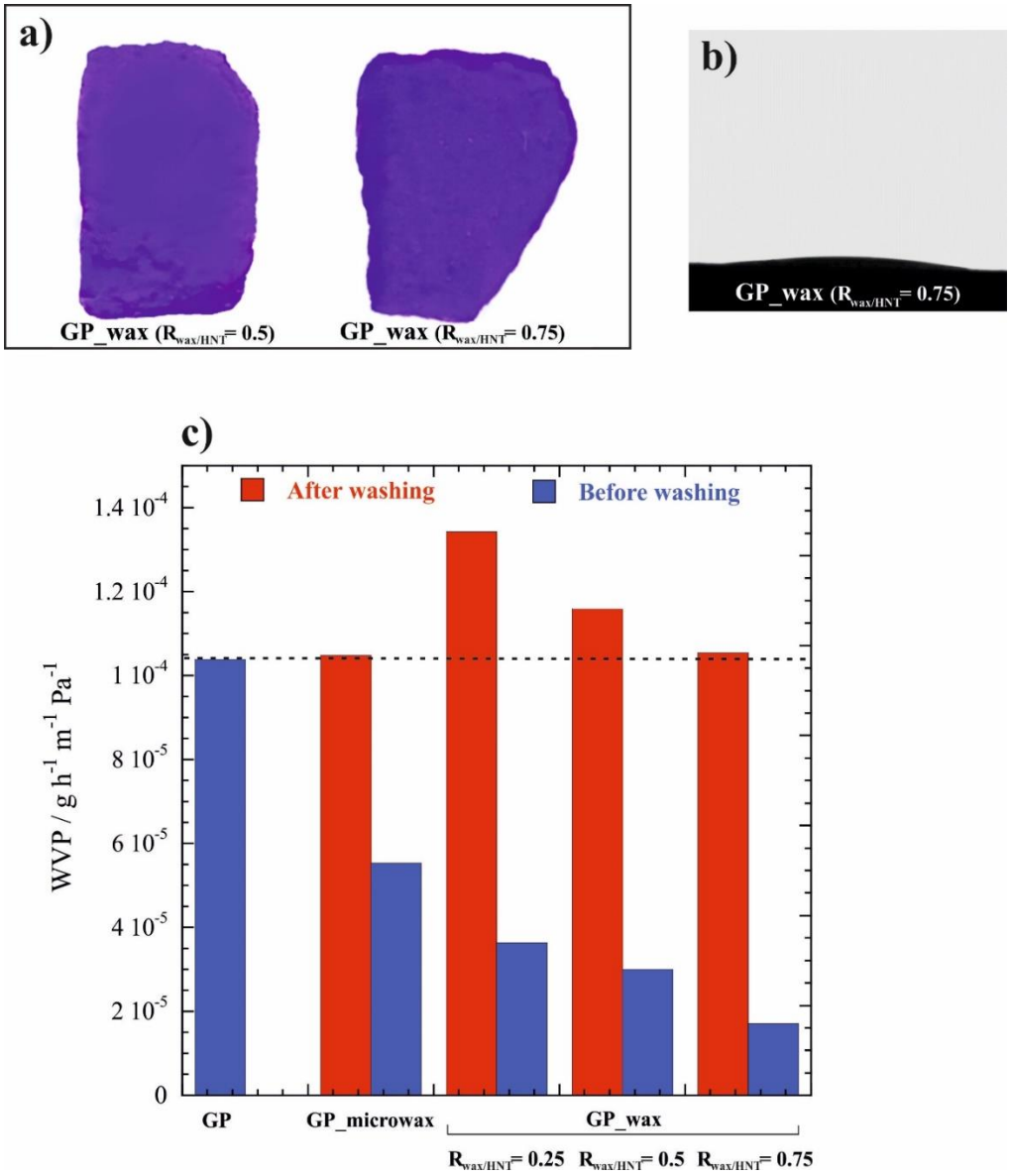

Figure 12. Comparison of Nile Red essay for GP_wax ($R_{wax/HNT}$ = 0.5 and 0.75) after their washing with ethanol (a). Image of the water droplet after its deposition on washed GP_wax ($R_{wax/HNT}$ = 0.75) (b). Water vapor permeability of GP material and filled geopolymers before and after wax removal. Dotted line represents WVP value of GP sample.

As expected, the washing procedure altered the wettability and the water vapor permeability properties of the filled geopolymers due to the wax removal. The complete wax removal was proved by the very hydrophilic character of the washed geopolymers. As example, the water droplet for washed GP_wax ($R_{wax/HNT}$ = 0.75) is presented in Figure 12b. The effect of the washing procedure on water vapor permeability of filled geopolymers are reported in Figure 12c. Prior to the geopolymer rinsing with ethanol, the presence of both wax and microwax induced a reduction of the water permeability compared with that of GP sample, which agrees with the surface hydrophobization

evidenced by the water contact angle data (Table 3). Specifically, the WVP results of the filled geopolymers could be attributed to the tortuosity effect as well as to decrease of geopolymer sorption sites for water molecules. Similar observations were detected for hydroxypropylcellulose films filled with wax microparticles [83]. On the other hand, an increase of the water permeability was observed after the rinsing step due to the actual removal of wax from the geopolymeric network (Figure 12c). Interestingly, the washed geopolymers evidenced different water permeability capacity on dependence of the initial wax content. The largest WVP value was determined for GP_wax ($R_{wax/HNT}$ = 0.25), which possess a significant higher water vapor permeability compared to that of GP material. The increase of $R_{wax/HNT}$ (0.5 and 0.75) allows us to obtain geopolymers with a lower WVP value after their washing with ethanol. Namely, we can state that GP_wax ($R_{wax/HNT}$ = 0.25) presents a higher porosity with respect to those of GP_wax ($R_{wax/HNT}$ = 0.5 and 0.75). As concerns GP_microwax, we detected that the rinsing with ethanol produced geopolymers with a water vapor permeability comparable with that of GP sample. On this basis, we can conclude that the removal of wax microparticles drives to the formation of geopolymeric materials with similar porosity respect to that of GP material. The latter was confirmed by helium pycnometer, which is a powerful technique to investigate the skeletal density and, consequently, the porosity of geopolymeric materials [74]. We observed that the incorporation of microwax within the HNT based geopolymer generates an increase of the skeletal density (2.27 ± 0.03 g cm^{-3} and 2.358 ± 0.011 g cm^{-3} for GP and GP_microwax, respectively) that can be attributed to a reduction of closed pores. This finding agrees with the flexural experiments, which evidenced that the stored energy up to breaking was enhanced by the filling of the geopolymer with microwax (Figure 11b). In this regard, literature reports that the mechanical performances of geopolymers based on kaolinite [84] and metakaolinite [74] can be improved by decreasing the volume of closed pores. We estimated that the porosity of GP_microwax (24.8 %) is significantly lower with respect to that of GP (49.9 %). The washing procedure did not alter the porosity of the unfilled geopolymer, while an enhancement up to 50.1 % was detected for GP_microwax sample confirming that the treatment by ethanol is effective to remove the microwax

particles from the geopolymer structure. The largest porosity (64.4 %) was detected for the washed GP_wax ($R_{wax/HNT}$ = 0.25) sample in agreement with its highest water vapor permeability (Figure 12b).

4. Conclusions

Hybrid geopolymers based on halloysite nanotubes and beeswax microspheres (diameter of ca. 3 – 5 μm) have been developed as natural materials suitable for engineering applications because of their flexibility and heat absorption capacity. Based on the thermogravimetric analyses, we estimated that the proposed protocol allowed us to obtain halloysite based geopolymers containing ca. 0.06 wt% of beeswax microparticles. Although the low amount of microwax, their loading within the geopolymeric network generated relevant improvements of the flexural characteristics and heat storage capacity with respect to the unfilled geopolymer. In this regard, the stored energy up to breaking was increased by a factor of 5. These effects can be attributed to the homogeneous distribution of microwax particles (obtained from the Pickering emulsion) within the geopolymeric matrix as evidenced by the structural characteristics and the morphology of the composite geopolymers.

For comparison, halloysite based geopolymers filled with variable amounts of beeswax were fabricated. Their properties are dependent on their composition, and they reflect the random dispersion of the beeswax. Relevant improvements of the flexibility and heat storage capacity can be achieved by adding a large amount (ca. 40 wt%) of beeswax. Namely, the filling with beeswax requires contents of ca. 1 order larger than the loading of microwax to obtain composite geopolymers with comparable performances.

Finally, we detected that both beeswax and microwax can be easily removed by washing the hybrid geopolymers with ethanol. Interestingly, the water vapour permeability of the washed geopolymers depends on the initial amount of wax incorporated in the geopolymeric network.

This work represents the starting point for the design of geopolymers filled with a phase change material (wax microparticles) that can act as smart thermal regulation systems for several applications within engineering and biotechnology.

Acknowledgments. The work was financially supported by "SETI-Sicilia Eco Tecnologie Innovative", Cod.Progetto 2017-NAZ-0204, PO FESR Sicilia 2014/2020 – Azione 1.1.5 and the University of Palermo.

Supplementary Material. DSC curves of Beeswax, GP_wax ($R_{wax/HNT}$ = 1) and GP_microwax. Thermogravimetric curve of GP_wax ($R_{wax/HNT}$ = 1) after washing. Assignment of IR peaks for geopolymer samples and halloysite.

References

[1] C. Garlisi, E. Trepci, X. Li, R. Al Sakkaf, K. Al-Ali, R.P. Nogueira, L. Zheng, E. Azar, G. Palmisano, Multilayer thin film structures for multifunctional glass: Self-cleaning, antireflective and energy-saving properties, Appl. Energy. 264 (2020) 114697. https://doi.org/10.1016/j.apenergy.2020.114697.

[2] A. Yusuf, S. Al Jitan, C. Garlisi, G. Palmisano, A review of recent and emerging antimicrobial nanomaterials in wastewater treatment applications, Chemosphere. 278 (2021) 130440. https://doi.org/10.1016/j.chemosphere.2021.130440.

[3] O. Jankovský, M. Lojka, A.-M. Lauermannová, F. Antončík, M. Pavlíková, M. Záleská, Z. Pavlík, A. Pivák, D. Sedmidubský, Towards novel building materials: High-strength nanocomposites based on graphene, graphite oxide and magnesium oxychloride, Appl. Mater. Today. 20 (2020) 100766. https://doi.org/10.1016/j.apmt.2020.100766.

[4] S. Saha, C. Rajasekaran, Enhancement of the properties of fly ash based geopolymer paste by incorporating ground granulated blast furnace slag, Constr. Build. Mater. 146 (2017) 615–620. https://doi.org/10.1016/j.conbuildmat.2017.04.139.

[5] Y. Luna-Galiano, C. Leiva, R. Villegas, F. Arroyo, L. Vilches, C. Fernández-Pereira, Carbon fiber waste incorporation in blast furnace slag geopolymer-composites, Mater. Lett. 233 (2018) 1–3. https://doi.org/10.1016/j.matlet.2018.08.099.

[6] Q. Wan, F. Rao, S. Song, C.A. León-Patiño, Geothermal clay-based geopolymer binders: Synthesis and microstructural characterization, Appl. Clay Sci. 146 (2017) 223–229. https://doi.org/10.1016/j.clay.2017.05.047.

[7] C. Ng, U.J. Alengaram, L.S. Wong, K.H. Mo, M.Z. Jumaat, S. Ramesh, A review on microstructural study and compressive strength of geopolymer mortar, paste and concrete, Constr. Build. Mater. 186 (2018) 550–576. https://doi.org/10.1016/j.conbuildmat.2018.07.075.

[8] Q. Su, Y. He, S. Yang, H. Wan, S. Chang, X. Cui, Synthesis of NaA-zeolite microspheres by conversion of geopolymer and their performance of Pb (II) removal, Appl. Clay Sci. 200 (2021) 105914. https://doi.org/10.1016/j.clay.2020.105914.

[9] M. El Alouani, H. Saufi, G. Moutaoukil, S. Alehyen, B. Nematollahi, W. Belmaghraoui, M. Taibi, Application of geopolymers for treatment of water contaminated with organic and inorganic pollutants: State-of-the-art review, J. Environ. Chem. Eng. 9 (2021) 105095. https://doi.org/10.1016/j.jece.2021.105095.

[10] K. Okada, A. Ooyama, T. Isobe, Y. Kameshima, A. Nakajima, K.J.D. MacKenzie, Water retention properties of porous geopolymers for use in cooling applications, J. Eur. Ceram. Soc. 29 (2009) 1917–1923. https://doi.org/10.1016/j.jeurceramsoc.2008.11.006.
[11] F. Aghabeyk, A. Azadmehr, A. Hezarkhani, Fabrication of feldspar-based geopolymers from perlite toward decontamination of heavy metals from aqueous solution: Hydrolysis process, characterizations, kinetic and isotherm studies, J. Environ. Chem. Eng. 10 (2022) 108087. https://doi.org/10.1016/j.jece.2022.108087.
[12] C. Bai, P. Colombo, Processing, properties and applications of highly porous geopolymers: A review, Ceram. Int. 44 (2018) 16103–16118. https://doi.org/10.1016/j.ceramint.2018.05.219.
[13] B.B. Jindal, R. Sharma, The effect of nanomaterials on properties of geopolymers derived from industrial by-products: A state-of-the-art review, Constr. Build. Mater. 252 (2020) 119028. https://doi.org/10.1016/j.conbuildmat.2020.119028.
[14] G.I. Fakhrullina, F.S. Akhatova, Y.M. Lvov, R.F. Fakhrullin, Toxicity of halloysite clay nanotubes in vivo: A Caenorhabditis elegans study, Environ. Sci. Nano. 2 (2015) 54–59. https://doi.org/10.1039/c4en00135d.
[15] M. Kryuchkova, A. Danilushkina, Y. Lvov, R. Fakhrullin, Evaluation of toxicity of nanoclays and graphene oxide: in vivo A Paramecium caudatum study, Environ. Sci. Nano. 3 (2016) 442–452. https://doi.org/10.1039/c5en00201j.
[16] E. Rozhina, S. Batasheva, R. Miftakhova, X. Yan, A. Vikulina, D. Volodkin, R. Fakhrullin, Comparative cytotoxicity of kaolinite, halloysite, multiwalled carbon nanotubes and graphene oxide, Appl. Clay Sci. 205 (2021) 106041. https://doi.org/10.1016/j.clay.2021.106041.
[17] Z. Long, Y.-P. Wu, H.-Y. Gao, J. Zhang, X. Ou, R.-R. He, M. Liu, In vitro and in vivo toxicity evaluation of halloysite nanotubes, J Mater Chem B. 6 (2018) 7204–7216. https://doi.org/10.1039/C8TB01382A.
[18] L.W. Wong, P. Pasbakhsh, A.M. Arabi, J. Keeling, J.B.L. Tan, Halloysite nanotubes from various geological deposits: New insights to acid etching and their impacts on products' characteristics, J. Environ. Chem. Eng. 9 (2021) 106235. https://doi.org/10.1016/j.jece.2021.106235.
[19] L. Lisuzzo, G. Cavallaro, S. Milioto, G. Lazzara, Halloysite nanotubes filled with MgO for paper reinforcement and deacidification, Appl. Clay Sci. 213 (2021). https://doi.org/10.1016/j.clay.2021.106231.
[20] L. Lisuzzo, G. Cavallaro, S. Milioto, G. Lazzara, Halloysite nanotubes as nanoreactors for heterogeneous micellar catalysis, J. Colloid Interface Sci. 608 (2022) 424–434. https://doi.org/10.1016/j.jcis.2021.09.146.
[21] Y. Zhao, E. Abdullayev, A. Vasiliev, Y. Lvov, Halloysite nanotubule clay for efficient water purification, J. Colloid Interface Sci. 406 (2013) 121–129. https://doi.org/10.1016/j.jcis.2013.05.072.
[22] Y. Song, P. Yuan, P. Du, L. Deng, Y. Wei, D. Liu, X. Zhong, J. Zhou, A novel halloysite–CeOx nanohybrid for efficient arsenic removal, Appl. Clay Sci. 186 (2020). https://doi.org/10.1016/j.clay.2020.105450.
[23] P. Maziarz, J. Matusik, A. Radziszewska, Halloysite-zero-valent iron nanocomposites for removal of Pb(II)/Cd(II) and As(V)/Cr(VI): Competitive effects, regeneration possibilities and mechanisms, J. Environ. Chem. Eng. 7 (2019) 103507. https://doi.org/10.1016/j.jece.2019.103507.
[24] S. Wang, D. Xiao, X. Zheng, L. Zheng, Y. Yang, H. Zhang, B. Ai, Z. Sheng, Halloysite and coconut shell biochar magnetic composites for the sorption of Pb(II) in wastewater: Synthesis, characterization and mechanism investigation, J. Environ. Chem. Eng. 9 (2021) 106865. https://doi.org/10.1016/j.jece.2021.106865.
[25] M.H. Kanani-Jazi, S. Akbari, Amino-dendritic and carboxyl functionalized halloysite nanotubes for highly efficient removal of cationic and anionic dyes: Kinetic, isotherm, and

thermodynamic studies, J. Environ. Chem. Eng. 9 (2021) 105214. https://doi.org/10.1016/j.jece.2021.105214.
[26] M. Amid, N. Nabian, M. Delavar, Performance evaluation and modeling study of PC blended membranes incorporated with SDS-modified and unmodified halloysite nanotubes in the separation of oil from water, J. Environ. Chem. Eng. 9 (2021) 105237. https://doi.org/10.1016/j.jece.2021.105237.
[27] S. Sadjadi, M.M. Heravi, S.S. Kazemi, Ionic liquid decorated chitosan hybridized with clay: A novel support for immobilizing Pd nanoparticles, Carbohydr. Polym. 200 (2018) 183–190. https://doi.org/10.1016/j.carbpol.2018.07.093.
[28] S. Sadjadi, M. Akbari, E. Monflier, M.M. Heravi, B. Leger, Pd nanoparticles immobilized on halloysite decorated with a cyclodextrin modified melamine-based polymer: a promising heterogeneous catalyst for hydrogenation of nitroarenes, New J Chem. 42 (2018) 15733–15742. https://doi.org/10.1039/C8NJ03014F.
[29] Y. Liu, H. Guan, J. Zhang, Y. Zhao, J.-H. Yang, B. Zhang, Polydopamine-coated halloysite nanotubes supported AgPd nanoalloy: An efficient catalyst for hydrolysis of ammonia borane, Int. J. Hydrog. Energy. 43 (2018) 2754–2762. https://doi.org/10.1016/j.ijhydene.2017.12.105.
[30] Y. Feng, X. Zhou, J. Yang, X. Gao, L. Yin, Y. Zhao, B. Zhang, Encapsulation of Ammonia Borane in Pd/Halloysite Nanotubes for Efficient Thermal Dehydrogenation, ACS Sustain. Chem. Eng. 8 (2020) 2122–2129. https://doi.org/10.1021/acssuschemeng.9b04480.
[31] A. Glotov, A. Vutolkina, A. Pimerzin, V. Vinokurov, Y. Lvov, Clay nanotube-metal core/shell catalysts for hydroprocesses, Chem Soc Rev. 50 (2021) 9240–9277. https://doi.org/10.1039/D1CS00502B.
[32] M. Liu, Y. Chang, J. Yang, Y. You, R. He, T. Chen, C. Zhou, Functionalized halloysite nanotube by chitosan grafting for drug delivery of curcumin to achieve enhanced anticancer efficacy, J. Mater. Chem. B. 4 (2016) 2253–2263. https://doi.org/10.1039/c5tb02725j.
[33] C. Cheng, Y. Gao, W. Song, Q. Zhao, H. Zhang, H. Zhang, Halloysite nanotube-based H2O2-responsive drug delivery system with a turn on effect on fluorescence for real-time monitoring, Chem. Eng. J. 380 (2020) 122474. https://doi.org/10.1016/j.cej.2019.122474.
[34] F. Liu, L. Bai, H. Zhang, H. Song, L. Hu, Y. Wu, X. Ba, Smart H2O2-Responsive Drug Delivery System Made by Halloysite Nanotubes and Carbohydrate Polymers, ACS Appl. Mater. Interfaces. 9 (2017) 31626–31633. https://doi.org/10.1021/acsami.7b10867.
[35] Y. Zhang, L. Bai, C. Cheng, Q. Zhou, Z. Zhang, Y. Wu, H. Zhang, A novel surface modification method upon halloysite nanotubes: A desirable cross-linking agent to construct hydrogels, Appl. Clay Sci. 182 (2019) 105259. https://doi.org/10.1016/j.clay.2019.105259.
[36] A. Vikulina, D. Voronin, R. Fakhrullin, V. Vinokurov, D. Volodkin, Naturally derived nano- and micro-drug delivery vehicles: halloysite, vaterite and nanocellulose, New J Chem. 44 (2020) 5638–5655. https://doi.org/10.1039/C9NJ06470B.
[37] G. Gorrasi, Dispersion of halloysite loaded with natural antimicrobials into pectins: Characterization and controlled release analysis, Carbohydr. Polym. 127 (2015) 47–53. https://doi.org/10.1016/j.carbpol.2015.03.050.
[38] M. Liu, C. Wu, Y. Jiao, S. Xiong, C. Zhou, Chitosan-halloysite nanotubes nanocomposite scaffolds for tissue engineering, J. Mater. Chem. B. 1 (2013) 2078–2089. https://doi.org/10.1039/c3tb20084a.
[39] M. Liu, R. Fakhrullin, A. Novikov, A. Panchal, Y. Lvov, Tubule Nanoclay-Organic Heterostructures for Biomedical Applications, Macromol. Biosci. 19 (2019) 1800419. https://doi.org/10.1002/mabi.201800419.
[40] J. Zhang, X. Luo, Y.-P. Wu, F. Wu, Y.-F. Li, R.-R. He, M. Liu, Rod in Tube: A Novel Nanoplatform for Highly Effective Chemo-Photothermal Combination Therapy toward Breast Cancer, ACS Appl. Mater. Interfaces. 11 (2019) 3690–3703. https://doi.org/10.1021/acsami.8b17533.

[41] A. Panchal, G. Fakhrullina, R. Fakhrullin, Y. Lvov, Self-assembly of clay nanotubes on hair surface for medical and cosmetic formulations, Nanoscale. 10 (2018) 18205–18216. https://doi.org/10.1039/C8NR05949G.
[42] G. Cavallaro, S. Milioto, S. Konnova, G. Fakhrullina, F. Akhatova, G. Lazzara, R. Fakhrullin, Y. Lvov, Halloysite/Keratin Nanocomposite for Human Hair Photoprotection Coating, ACS Appl. Mater. Interfaces. 12 (2020) 24348–24362. https://doi.org/10.1021/acsami.0c05252.
[43] A. Panchal, G. Fakhrullina, R. Fakhrullin, Y. Lvov, Self-assembly of clay nanotubes on hair surface for medical and cosmetic formulations, Nanoscale. 10 (2018) 18205–18216. https://doi.org/10.1039/c8nr05949g.
[44] M. Gruppuso, G. Turco, E. Marsich, D. Porrelli, Polymeric wound dressings, an insight into polysaccharide-based electrospun membranes, Appl. Mater. Today. 24 (2021) 101148. https://doi.org/10.1016/j.apmt.2021.101148.
[45] B. Zhang, H. Guo, P. Yuan, Y. Li, Q. Wang, L. Deng, D. Liu, Geopolymerization of halloysite via alkali-activation: Dependence of microstructures on precalcination, Appl. Clay Sci. 185 (2020) 105375. https://doi.org/10.1016/j.clay.2019.105375.
[46] M. Razzaghian Ghadikolaee, A. Habibnejad Korayem, A. Sharif, Y. Ming Liu, The halloysite nanotube effects on workability, mechanical properties, permeability and microstructure of cementitious mortar, Constr. Build. Mater. 267 (2021) 120873. https://doi.org/10.1016/j.conbuildmat.2020.120873.
[47] B. Zhang, H. Guo, P. Yuan, L. Deng, X. Zhong, Y. Li, Q. Wang, D. Liu, Novel acid-based geopolymer synthesized from nanosized tubular halloysite: The role of precalcination temperature and phosphoric acid concentration, Cem. Concr. Compos. 110 (2020) 103601. https://doi.org/10.1016/j.cemconcomp.2020.103601.
[48] M.M. Calvino, G. Cavallaro, L. Lisuzzo, S. Milioto, G. Lazzara, Separation of halloysite/kaolinite mixtures in water controlled by sucrose addition: The influence of the attractive forces on the sedimentation behavior, Colloids Surf. Physicochem. Eng. Asp. 641 (2022) 128530. https://doi.org/10.1016/j.colsurfa.2022.128530.
[49] Z. Zhang, H. Wang, X. Yao, Y. Zhu, Effects of halloysite in kaolin on the formation and properties of geopolymers, Cem. Concr. Compos. 34 (2012) 709–715. https://doi.org/10.1016/j.cemconcomp.2012.02.003.
[50] L. Lisuzzo, G. Cavallaro, S. Milioto, G. Lazzara, Pickering Emulsions Stabilized by Halloysite Nanotubes: From General Aspects to Technological Applications, Adv. Mater. Interfaces. (2022) 2102346–2102375. https://doi.org/10.1002/admi.202102346.
[51] D. Stehl, T. Skale, L. Hohl, Y. Lvov, J. Koetz, M. Kraume, A. Drews, R. Von Klitzing, Oil-in-Water Pickering Emulsions Stabilized by Halloysite Clay Nanotubes Toward Efficient Filterability, ACS Appl. Nano Mater. 3 (2020) 11743–11751. https://doi.org/10.1021/acsanm.0c02205.
[52] T. Yu, L.T. Swientoniewski, M. Omarova, M.-C. Li, I.I. Negulescu, N. Jiang, O.A. Darvish, A. Panchal, D.A. Blake, Q. Wu, Y.M. Lvov, V.T. John, D. Zhang, Investigation of Amphiphilic Polypeptoid-Functionalized Halloysite Nanotubes as Emulsion Stabilizer for Oil Spill Remediation, ACS Appl. Mater. Interfaces. 11 (2019) 27944–27953. https://doi.org/10.1021/acsami.9b08623.
[53] O. Owoseni, Y. Su, S. Raghavan, A. Bose, V.T. John, Hydrophobically modified chitosan biopolymer connects halloysite nanotubes at the oil-water interface as complementary pair for stabilizing oil droplets, J. Colloid Interface Sci. 620 (2022) 135–143. https://doi.org/10.1016/j.jcis.2022.03.142.
[54] C. Ferone, G. Roviello, F. Colangelo, R. Cioffi, O. Tarallo, Novel hybrid organic-geopolymer materials, Appl. Clay Sci. 73 (2013) 42–50. https://doi.org/10.1016/j.clay.2012.11.001.
[55] R. Mustafa, K.N. Shivaprasad, B.B. Das, Effect of various additives on the properties of fly ash based geopolymer mortar, Lect. Notes Civ. Eng. 25 (2019) 707–715. https://doi.org/10.1007/978-981-13-3317-0_63.

[56] E. Prud'homme, P. Michaud, S. Rossignol, E. Joussein, Mechanical properties of geopolymer composite reinforced by organic or inorganic additives, in: 2014: pp. 67–78.
[57] P. Behera, V. Baheti, J. Militky, P. Louda, Elevated temperature properties of basalt microfibril filled geopolymer composites, Constr. Build. Mater. 163 (2018) 850–860. https://doi.org/10.1016/j.conbuildmat.2017.12.152.
[58] Q. Han, P. Zhang, J. Wu, Y. Jing, D. Zhang, T. Zhang, Comprehensive review of the properties of fly ash-based geopolymer with additive of nano-SiO2, Nanotechnol. Rev. 11 (2022) 1478–1498. https://doi.org/10.1515/ntrev-2022-0092.
[59] A. Karthik, K. Sudalaimani, C.T. Vijayakumar, Durability study on coal fly ash-blast furnace slag geopolymer concretes with bio-additives, Ceram. Int. 43 (2017) 11935–11943. https://doi.org/10.1016/j.ceramint.2017.06.042.
[60] P. Khamlue, N. Lertcumfu, P. Jaita, S. Manotham, T. Tunkasiri, P. Malasri, G. Rujijanagul, The effects of Biochar additive on the properties of Geopolymer materials, Key Eng. Mater. 798 KEM (2019) 273–278. https://doi.org/10.4028/www.scientific.net/KEM.798.273.
[61] S.K. John, Y. Nadir, K. Girija, Effect of source materials, additives on the mechanical properties and durability of fly ash and fly ash-slag geopolymer mortar: A review, Constr. Build. Mater. 280 (2021) 122443. https://doi.org/10.1016/j.conbuildmat.2021.122443.
[62] P. F. De Castro, S. Minko, V. Vinokurov, K. Cherednichenko, D.G. Shchukin, Long-Term Autonomic Thermoregulating Fabrics Based on Microencapsulated Phase Change Materials, ACS Appl. Energy Mater. 4 (2021) 12789–12797. https://doi.org/10.1021/acsaem.1c02170.
[63] E.M. Shchukina, M. Graham, Z. Zheng, D.G. Shchukin, Nanoencapsulation of phase change materials for advanced thermal energy storage systems, Chem. Soc. Rev. 47 (2018) 4156–4175. https://doi.org/10.1039/C8CS00099A.
[64] Z. Zheng, Z. Chang, G.-K. Xu, F. McBride, A. Ho, Z. Zhuola, M. Michailidis, W. Li, R. Raval, R. Akhtar, D. Shchukin, Microencapsulated Phase Change Materials in Solar-Thermal Conversion Systems: Understanding Geometry-Dependent Heating Efficiency and System Reliability, ACS Nano. 11 (2017) 721–729. https://doi.org/10.1021/acsnano.6b07126.
[65] L. Lisuzzo, T. Hueckel, G. Cavallaro, S. Sacanna, G. Lazzara, Pickering Emulsions Based on Wax and Halloysite Nanotubes: An Ecofriendly Protocol for the Treatment of Archeological Woods, ACS Appl. Mater. Interfaces. 13 (2021) 1651–1661. https://doi.org/10.1021/acsami.0c20443.
[66] C. Duce, S. Vecchio Ciprioti, L. Ghezzi, V. Ierardi, M.R. Tinè, Thermal behavior study of pristine and modified halloysite nanotubes: A modern kinetic study, J. Therm. Anal. Calorim. 121 (2015) 1011–1019. https://doi.org/10.1007/s10973-015-4741-7.
[67] Z. Sun, Y. Zhang, S. Zheng, Y. Park, R.L. Frost, Preparation and thermal energy storage properties of paraffin/calcined diatomite composites as form-stable phase change materials, Thermochim. Acta. 558 (2013) 16–21. https://doi.org/10.1016/j.tca.2013.02.005.
[68] Y. Zhao, S. Thapa, L. Weiss, Y. Lvov, Phase Change Heat Insulation Based on Wax-Clay Nanotube Composites, Adv. Eng. Mater. 16 (2014) 1391–1399. https://doi.org/10.1002/adem.201400094.
[69] J. Zhang, X. Zhang, Y. Wan, D. Mei, B. Zhang, Preparation and thermal energy properties of paraffin/halloysite nanotube composite as form-stable phase change material, Sol. Energy. 86 (2012) 1142–1148. https://doi.org/10.1016/j.solener.2012.01.002.
[70] M. Catauro, G. Dal Poggetto, C. Sgarlata, S. Vecchio Ciprioti, S. Pacifico, C. Leonelli, Thermal and microbiological performance of metakaolin-based geopolymers cement with waste glass, Appl. Clay Sci. 197 (2020) 105763. https://doi.org/10.1016/j.clay.2020.105763.
[71] A. Hajimohammadi, J.L. Provis, J.S.J. van Deventer, Time-resolved and spatially-resolved infrared spectroscopic observation of seeded nucleation controlling geopolymer gel formation, J. Colloid Interface Sci. 357 (2011) 384–392. https://doi.org/10.1016/j.jcis.2011.02.045.

[72] M.R. El-Naggar, M.I. El-Dessouky, Re-use of waste glass in improving properties of metakaolin-based geopolymers: Mechanical and microstructure examinations, Constr. Build. Mater. 132 (2017) 543–555. https://doi.org/10.1016/j.conbuildmat.2016.12.023.
[73] A. Fernández-Jiménez, A. Palomo, J.Y. Pastor, A. Martín, New Cementitious Materials Based on Alkali-Activated Fly Ash: Performance at High Temperatures, J. Am. Ceram. Soc. 91 (2008) 3308–3314. https://doi.org/10.1111/j.1551-2916.2008.02625.x.
[74] F.G.M. Aredes, T.M.B. Campos, J.P.B. Machado, K.K. Sakane, G.P. Thim, D.D. Brunelli, Effect of cure temperature on the formation of metakaolinite-based geopolymer, Ceram. Int. 41 (2015) 7302–7311. https://doi.org/10.1016/j.ceramint.2015.02.022.
[75] N. Tanner, B. Lichtenberg- Kraag, Identification and Quantification of Single and Multi-Adulteration of Beeswax by FTIR- ATR Spectroscopy, Eur. J. Lipid Sci. Technol. 121 (2019) 1900245. https://doi.org/10.1002/ejlt.201900245.
[76] S. Greiser, P. Sturm, G.J.G. Gluth, M. Hunger, C. Jäger, Differentiation of the solid-state NMR signals of gel, zeolite phases and water species in geopolymer-zeolite composites, Ceram. Int. 43 (2017) 2202–2208. https://doi.org/10.1016/j.ceramint.2016.11.004.
[77] C.R. Kaze, A. Nana, G.L. Lecomte-Nana, J.G.N. Deutou, E. Kamseu, U.C. Melo, F. Andreola, C. Leonelli, Thermal behaviour and microstructural evolution of metakaolin and meta-halloysite-based geopolymer binders: a comparative study, J. Therm. Anal. Calorim. 147 (2022) 2055–2071. https://doi.org/10.1007/s10973-021-10555-2.
[78] A.Z. Khalifa, Ö. Cizer, Y. Pontikes, A. Heath, P. Patureau, S.A. Bernal, A.T.M. Marsh, Advances in alkali-activation of clay minerals, Cem. Concr. Res. 132 (2020) 106050. https://doi.org/10.1016/j.cemconres.2020.106050.
[79] A. Bucio, R. Moreno-Tovar, L. Bucio, J. Espinosa-Dávila, F. Anguebes-Franceschi, Characterization of Beeswax, Candelilla Wax and Paraffin Wax for Coating Cheeses, Coatings. 11 (2021) 261. https://doi.org/10.3390/coatings11030261.
[80] S. Naderizadeh, J.A. Heredia-Guerrero, G. Caputo, S. Grasselli, A. Malchiodi, A. Athanassiou, I.S. Bayer, Superhydrophobic Coatings from Beeswax-in-Water Emulsions with Latent Heat Storage Capability, Adv. Mater. Interfaces. 6 (2019) 1801782. https://doi.org/10.1002/admi.201801782.
[81] Y. Gaillard, A. Mija, A. Burr, E. Darque-Ceretti, E. Felder, N. Sbirrazzuoli, Green material composites from renewable resources: Polymorphic transitions and phase diagram of beeswax/rosin resin, Thermochim. Acta. 521 (2011) 90–97. https://doi.org/10.1016/j.tca.2011.04.010.
[82] V.A. Cataldo, G. Cavallaro, G. Lazzara, S. Milioto, F. Parisi, Coffee grounds as filler for pectin: Green composites with competitive performances dependent on the UV irradiation, Carbohydr. Polym. 170 (2017) 198–205. https://doi.org/10.1016/j.carbpol.2017.04.092.
[83] L. Lisuzzo, M.R. Caruso, G. Cavallaro, S. Milioto, G. Lazzara, Hydroxypropyl Cellulose Films Filled with Halloysite Nanotubes/Wax Hybrid Microspheres, Ind. Eng. Chem. Res. 60 (2021) 1656–1665. https://doi.org/10.1021/acs.iecr.0c05148.
[84] W. Sornlar, A. Wannagon, S. Supothina, Stabilized homogeneous porous structure and pore type effects on the properties of lightweight kaolinite-based geopolymers, J. Build. Eng. 44 (2021) 103273. https://doi.org/10.1016/j.jobe.2021.103273.

Graphical Abstract

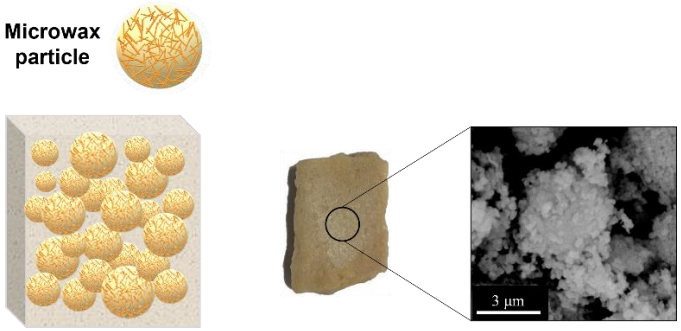

Geopolymer filled with microwax